Magnetocaloric effect and critical exponent studies in $Mn_{4.5}Ni_{0.5}Sn_3$ alloy

Nagalakshmi R*

Intermetallics and Non-linear optics laboratory
Department of Physics
National Institute of Technology
Tiruchirappalli 620 015, India

Received 10 June 2020

Abstract: Magnetic refrigeration is a promising alternative cooling technology as it is non-polluting and more efficient than gas compression system. In this article we have reviewed the magnetocaloric properties of $Mn_{4.5}Ni_{0.5}Sn_3$ alloy. Its crystal structure is found to be hexagonal Ni_2In-type (space group = $P63/mmc$). The alloy undergoes second order ferromagnetic transition at T_C = 180 K. $Mn_{4.5}Ni_{0.5}Sn_3$ alloy is a moderate heavy Fermion and exhibits bad metallic nature as a consequence of strong impurity scattering. From the critical analysis, presence of long range interaction in the alloy is well established as the critical exponents' values are close to the theoretical values of mean field model. Further magnetocaloric studies reveal a maximum magnetic entropy change of 1.87 J/kg K with a wide working span, ΔT = 86 K yielding a relative cooling power (RCP) of 160 J/kg for a field change of 0 - 5 T.

Key words: Critical exponents, Magnetocaloric effect, Moderate heavy Fermion, Relative cooling power

1 Introduction

In the current scenario, global energy demand, environmental pollution, global warming being pressing issues, it is inevitable to develop innovative green technologies especially in refrigeration area. Magnetic refrigeration is one such technology which employs non-polluting, magnetic field cooled refrigerants and reduces

*Recipient of Saraswathy Srinivasan Prize: Young Scientist Award in Physics (2019)
Email: nagaphys@yahoo.com

the power consumption by 30-40% when compared to the conventional refrigerators. In the past couple of decades, a great progress in magnetic refrigeration has been witnessed, and today, it has attained a level of commercialization. As far as magnetic refrigerants are concerned, rare earth based intermetallic alloys are considered as prime candidates, but economically, they are not compatible and also most of the rare earth based alloys magnetically order at low temperatures[1-3]. So, the exploration of transition metal-based alloys has given a new momentum for finding novel magnetocaloric materials which are more feasible in application point of view. Especially, manganese is more suitable than other transition elements because it is cheaper, highly abundant and possesses higher magnetic moment [4,5]. In addition, materials exhibiting second order magnetic transition are desirable, as they exhibit negligible thermal or magnetic hysteresis and hence higher relative cooling power (RCP). Moreover, most of the Mn based alloys such as MnTX (T = Co, Ni; X = Ge, Si) [6-11], NiMn based Heusler alloys [1,12], Mn_5Sn_3 based alloys [13,14] show near room temperature magnetocaloric effect (MCE). Among them, Mn_5Sn_3 is unique because, it exhibits two Mn-rich magnetic sub-lattices each ordering at different temperatures [15]. As a consequence, dual peak is observed in magnetic entropy change ($-\Delta S_M$) leading to a wide temperature MCE. Another advantage of these materials is that their magnetic properties can be easily tuned via doping with foreign magnetic or non-magnetic atoms. Many such studies have been previously reported on $Mn_5Sn_{3-x}Ga_x$ [13], $(Mn_{1-x}Fe_x)_5Sn_3$ [14] and $Mn_5(Sn_{1-x}Sb_x)_3$ [15] from which the influence of doping on magnetic interactions and MCE magnitude can be realized.

There exists a handful of theoretical methods to explore the underlying principle and properties of MCE materials. Critical exponent analysis is one of the best methods, which explains magnetic properties near critical temperature of a second order magnetic material through well known theoretical models. With the help of fundamental thermodynamics and statistical mechanics, scaling relation and critical exponents for a particular system can be derived, using which, nature of magnetic interactions are studied with deeper insight. From the critical exponent analysis, it is found that certain alloys like $MnCo_{1-x}Sn_xGe$ [16], $Mn_{1-x}CoGeSi_x$ [17], $MnCo_{1-x}Nb_xGe$ [18], $MnCo_{1-x}Ti_xGe$ [19] with x = 0.02, 0.04, 0.06, 0.08 obey molecular field model. On the other hand, $Mn_4FeGe_{3-x}Si_x$ [20] (x = 0.0, 0.2,0.6,1) obeys short-range 3D-Heisenberg model below T_C and long-range molecular field model above T_C.

So far, critical exponent analysis has not been reported in Mn_5Sn_3 systems in which the nature of the magnetic interaction is unclear. We have synthesized a novel alloy, $Mn_{4.5}Ni_{0.5}Sn_3$, and have studied its fundamental properties. Further, we have analyzed its magnetocaloric properties from which the system is found to show wide temperature span with ΔT = 86 K [21]. In this article we have reviewed the outcome of the above work.

2 Experimental Details

Arc melting technique was used to prepare polycrystalline $Mn_{4.5}Ni_{0.5}Sn_3$ alloy. Appropriate amounts of high purity Mn (99.95 %), Ni (99.99 %) and Sn (99.999 %) pieces were taken as starting elements in copper hearth of tri arc furnace and melted under Ar atmosphere. The so obtained ingot was turned over and remelted five times to enhance the homogeneity of the alloy. The prepared ingot was subsequently sealed in a vacuum quartz tube and annealed at 800^o C for 5 days. A small piece of the sample was crushed into fine powder to record room temperature X-ray diffraction (XRD) in the range of $20^o \leq 2\theta \leq 80^o$ using Panalytical Xpert PRO X-Ray Diffractometer with Cu-K_a radiation (λ = 1.54056 Å) and Rietveld refinement was performed to estimate the crystallographic parameters. Compositional homogeneity and phase purity of the alloy were ensured from BSE images recorded using SEM equipped EDAX. The thermomagnetic curves were obtained in both field cooled (FC) and zero field cooled (ZFC) protocols and the isothermal magnetization measurements were performed using DYNACOOL device of Quantum Design in a magnetic field upto 9 T and in the temperature range of 2 - 300 K. The electrical resistivity and the heat capacity of the sample were measured in DYNACOOL device of Quantum Design using four probe method and relaxation technique, respectively.

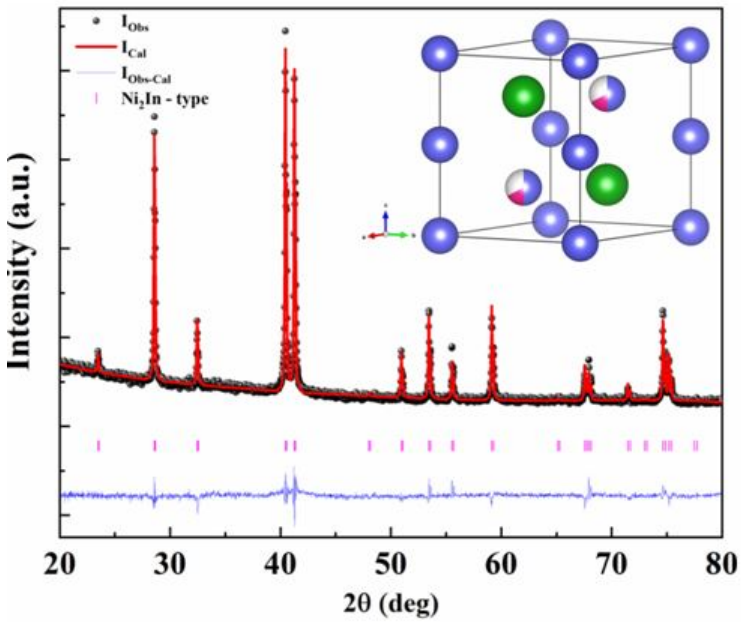

Fig. 1. Rietveld refined X-ray diffraction pattern of $Mn_{4.5}Ni_{0.5}Sn_3$ alloy. Inset shows a unit cell of $Mn_{4.5}Ni_{0.5}Sn_3$ alloy where violet, green and pink shades represent Mn, Sn and Ni atoms respectively.

3 Results and discussion

The crystal structure of $Mn_{4.5}Ni_{0.5}Sn_3$ alloy is found to be hexagonal Ni_2In-type (space group = $P63/mmc$) and from the Rietveld Refinement performed using FULLPROF SUITE software [22], the lattice parameters are determined as $a = 4.3732(6)$ Å and $c = 5.5136(1)$ Å. In $Mn_{4.5}Ni_{0.5}Sn_3$ alloy, 2a site (0, 0, 0) and 2c site (1/3, 2/3, 1/4) are occupied by MnI and Sn atoms. MnII (50 %) and Ni (17 %) atoms, while the rest being vacant [23,24]. The nominal composition and phase purity of the as prepared alloy have been identified using EDS analysis along with BSE measurement as displayed in Fig.2. From the image, it is evident that the alloy has crystallized in single phase along with traces of manganese. The results obtained from EDS analysis are shown in Table. I.

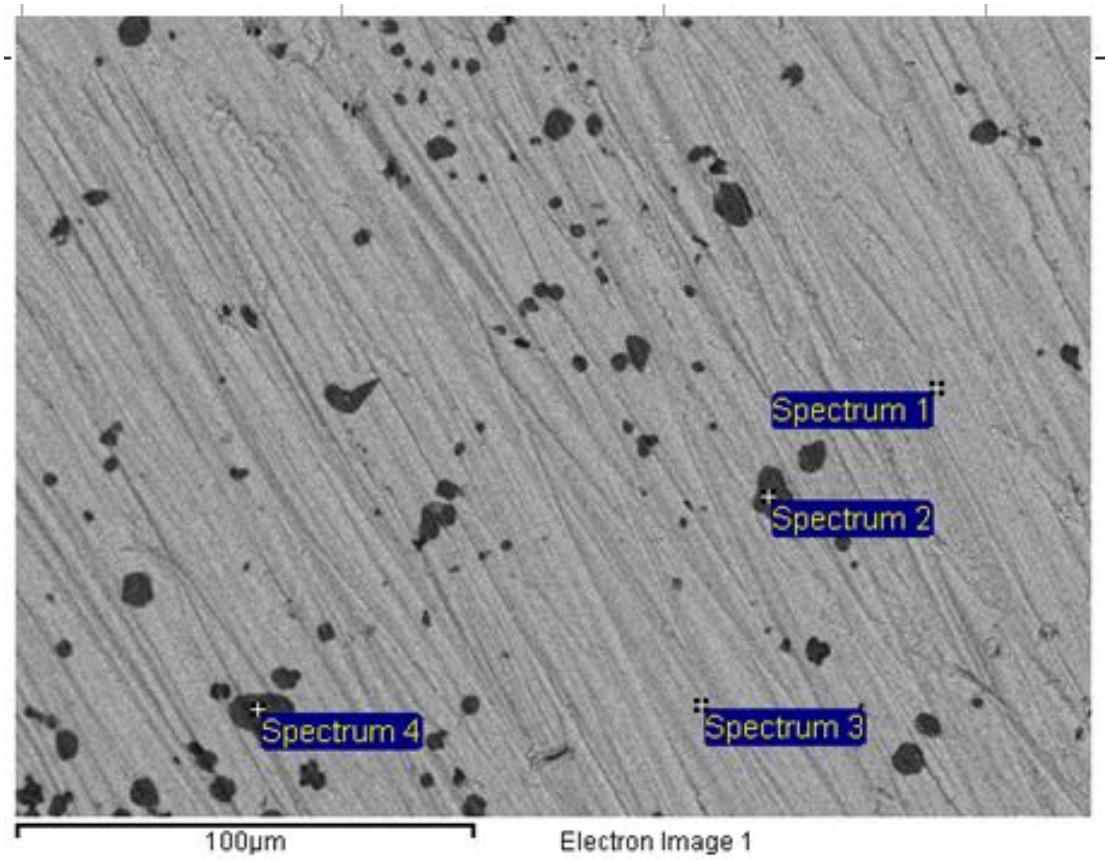

Fig. 2. BSE image of $Mn_{4.5}Ni_{0.5}Sn_3$ alloy

Table 1: EDS results of $Mn_{4.5}Ni_{0.5}Sn_3$ alloy

Contrast label	Composition (at. %)			Phase
	Mn	Ni	Sn	
Spectrum 1	54.80	6.06	39.15	$Mn_{4.5}Ni_{0.5}Sn_3$
Spectrum 2	99.42	0.00	0.58	Mn
Spectrum 3	55.34	5.89	38.77	$Mn_{4.5}Ni_{0.5}Sn_3$
Spectrum 4	99.49	0.00	0.51	Mn

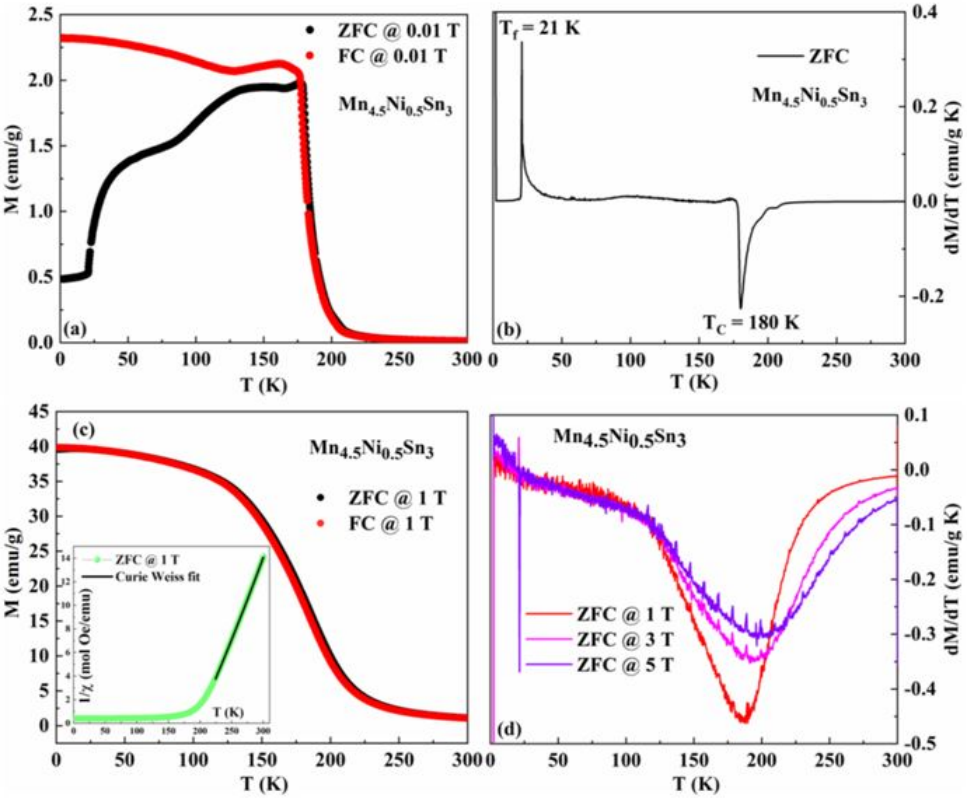

Fig.3. (a) Temperature dependent magnetization (M(T)) in an applied magnetic field of B = 0.01 T in both ZFC and FC modes; (b) first derivative of M(T) at B = 0.01 T; (c) M(T) at B = 1 T. Inset shows fit of Curie Weiss equation in inverse susceptibility data (d) First derivative of M(T) at various magnetic fields.

ZFC and FC thermomagnetic curves measured in B = 0.01 T are shown in Fig. 3(a). Here, a sharp increase in magnetization around Curie temperature, T_C = 180 K (identified from the minimum in dM/dT as shown in Fig 3(b)) indicates paramagnetic-ferromagnetic transition. The bifurcation between ZFC and FC curves around 175 K is due to pinning of domain walls. At T_f = 21 K, ZFC shows a slope change due to spin freezing transition. Many Mn-Sn systems are found to show this characteristic because of their reentrant spin glass behavior which arises due to frustration and randomness within the spin system [15,25,26]. This might also be the root cause of the large bifurcation noted in the system. At B = 1 T, both the curves reveal a typical ferromagnetic behavior without irreversibility. On performing Curie-Weiss fitting (inset of Fig 3(c)), $\chi(T) = C/(T - \theta_{CW})$, we determined the Curie-Weiss temperature (θ_{CW}) and effective paramagnetic moment of the system (μ_{eff}) as 194 K and 3.83 μ_B, respectively. Shift in extrema in the derivative of ZFC magnetization towards the positive T-direction with increasing field further corroborates the ferromagnetic nature of the transition (Fig 3(d)).

The isothermal magnetization measurements around Curie temperature are illustrated in Fig. 4.

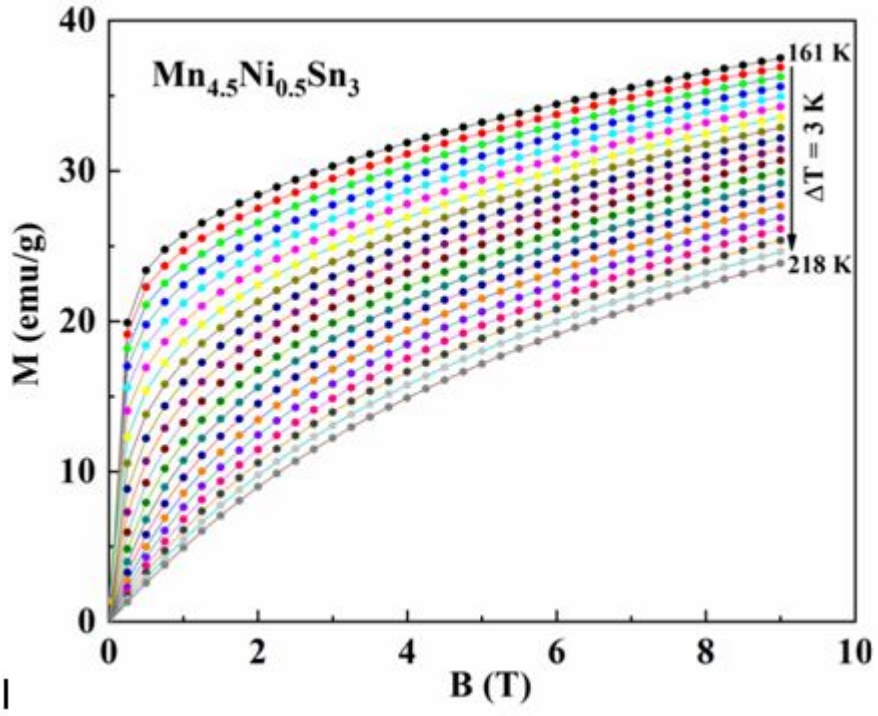

Fig. 4: Field dependent magnetization of $Mn_{4.5}Ni_{0.5}Sn_3$ alloy

Landau expansion of Gibbs free energy can be written as,

$$G(M,T) = G_0\frac{1}{2}C_1(T)M^2 + \frac{1}{4}C_2(T)M^4 + \frac{1}{6}C_3(T)M^6 + \cdots - MB \tag{1}$$

where $C_1(T)$, $C_2(T)$ and $C_3(T)$ are temperature dependent parameters referred as Landau coefficients. At equilibrium condition, $\partial G/\partial M = 0$, the magnetic equation of state becomes,

$$\frac{B}{M} = C_1(T) + C_2(T)M^2 \tag{2}$$

$C_(T)$ and $C_2(T)$ of the above equation can be obtained by fitting Eq. (2) in the linear region of the Arrott plot. In general, $C_1(T)$ grows with temperature exhibiting a sign change around T_C. Whereas, the other parameter $C_2(T)$ is usually positive at T_C in case of second order magnetic transition and negative for first order magnetic transition [17]. From Fig. 5, it can be clearly seen that, $C_2(T)$ is positive around T_C pointing out the second order magnetic nature of the alloy.

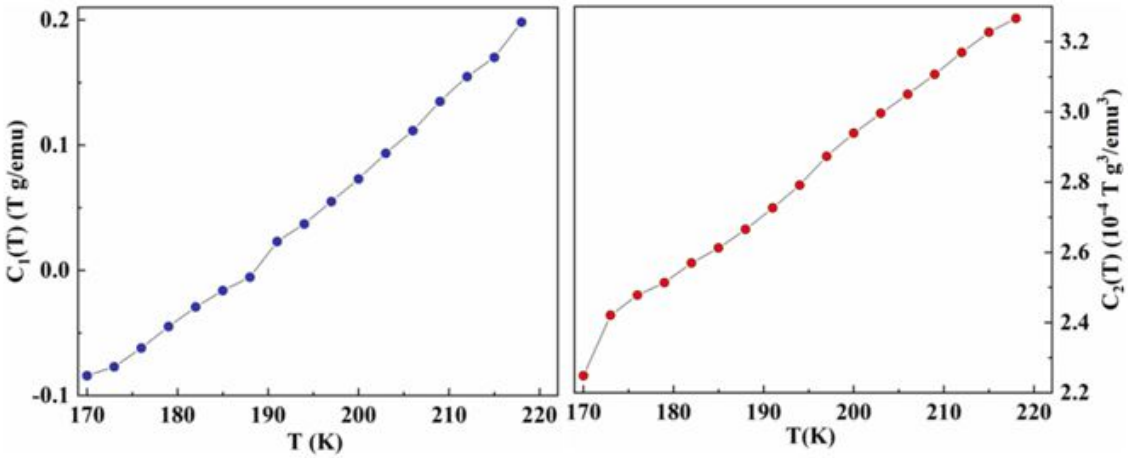

Fig. 5. Temperature dependent parameters A(T) and B(T) of $Mn_{4.5}Ni_{0.5}Sn_3$ alloy

3.1 Critical Exponent Analysis:

To understand the complex magnetic behavior and the nature of the transition present in the alloy, critical behavior of $Mn_{4.5}Ni_{0.5}Sn_3$ alloy around T_C has been analyzed based on well- known theoretical models. We have opted different methods like Modified Arrott plot (MAP), Kouvel-Fisher method (KF) and Critical Isotherms to find the critical exponents (γ, β and δ). From the isothermal magnetization, we have derived the modified Arrott plot using Arrott-Noakes equation of state [27],

$$(B/M)^{1/\gamma} = (T - T_C)/T + M^{1/\beta}. \tag{3}$$

Arrott plots constructed for four different models: Mean field model ($\beta = 0.365; \gamma = 1.336$) [28], 3D Heisenberg model ($\beta = 0.365; \gamma = 1.336$) [28], 3D Ising-model ($\beta = 0.325; \gamma = 1.241$) [28] and Tricritical mean field model ($\beta = 0.25; \gamma = 1$) [29] is presented in Fig. 6. It can be clearly seen that, all the curves pertaining to Mean field model are parallel to each other at higher fields around T_C, unlike the other models where clear deviation from linearity is evident.

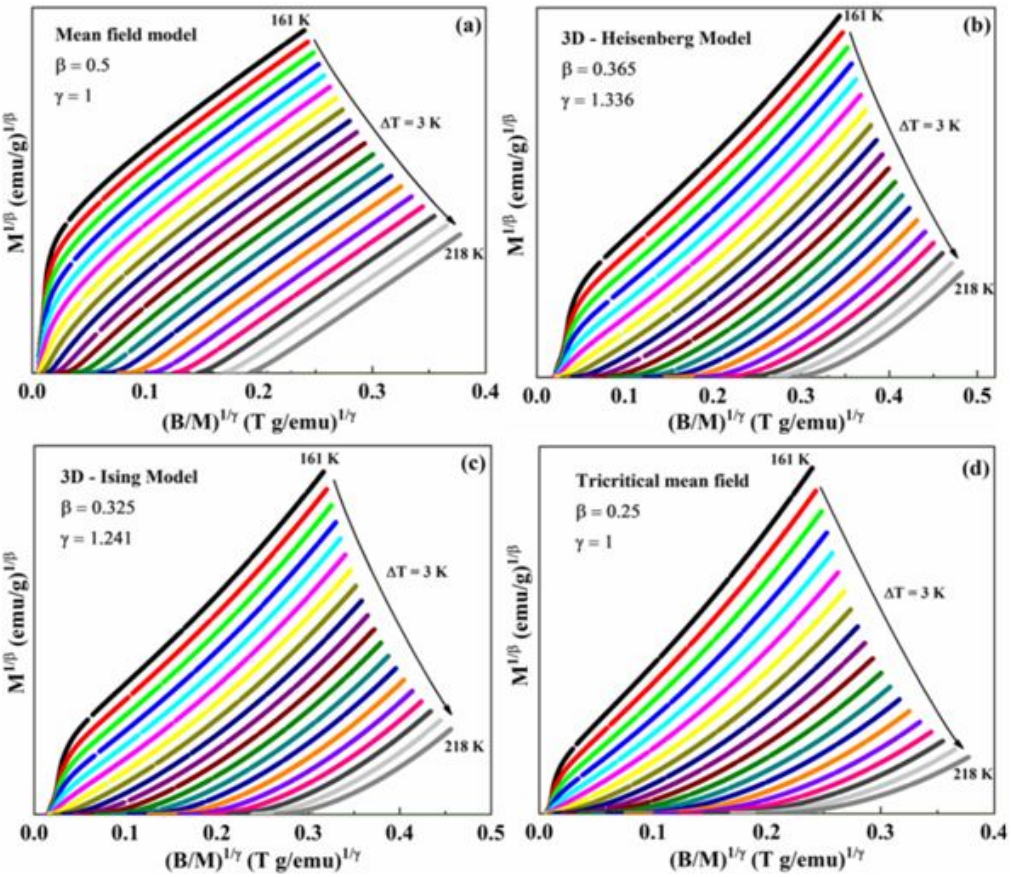

Fig. 6. Modified Arrott plots of $Mn_{4.5}Ni_{0.5}Sn_3$ alloy

In order to identify the most appropriate model, we have determined relative slope (RS) which is described as $RS = S(T)/S(T_C)$, here $S(T)$ denotes slope of the curves at various temperatures and $S(T_C)$ is slope at T_C. From Fig. 7 we could conclude that, the Mean field model is more appropriate to the system since the value of RS is closer to 1.

The spontaneous magnetization (M_S) and initial susceptibility (χ_0^{-1}) are obtained by extrapolating the linear high field region of mean field MAP curves below

and above T_C respectively. The so derived values are plotted against temperature and fitted with power law equation (Fig. 8(a)) stated below [30],

$$M_S = \lim_{B\to 0} M = M_0[(T_C - T)/T_C]^{\beta}, \quad \text{for } T < T_C. \tag{4}$$

$$\chi_0^{-1} = \lim_{B\to 0}\left(\frac{B}{M}\right) = \left(\frac{h_0}{m_0}\right)[(T - T_C)/T_C]^{\gamma}, \quad \text{for } T > T_C. \tag{5}$$

Here h_0/m_0 and M_0 are critical amplitudes. The above fitting has yielded the following critical parameters: $\beta = 0.494(6)$ with $T_C = 189.8(3)$ K and $\gamma = 1.065(1)$ with $T_C = 189.6(1)$ K. The obtained results coincide well with mean field model.

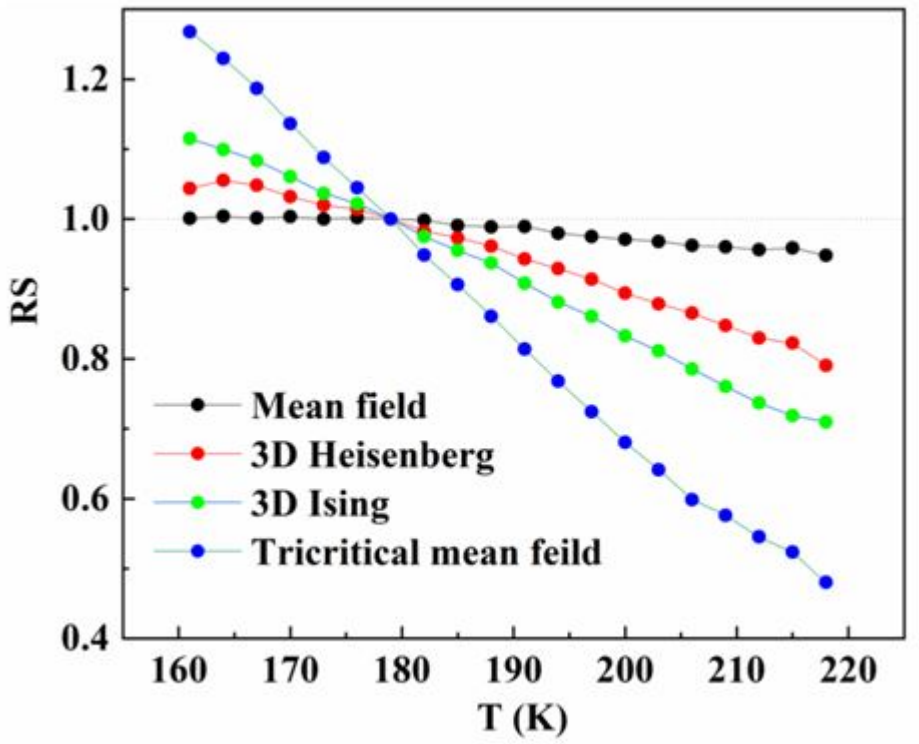

Fig. 7. Relative slope of modified Arrott curves as a function of temperature

A more accurate technique to determine the critical exponents is Kouvel-Fisher method [31], which is based on the following equations,

$$\frac{M_S(T)}{dM_S(T)/dT} = \frac{T - T_C}{\beta} \tag{6}$$

$$\frac{\chi_0^{-1}(T)}{d\chi_0^{-1}(T)/dT} = \frac{T - T_C}{\gamma} \tag{7}$$

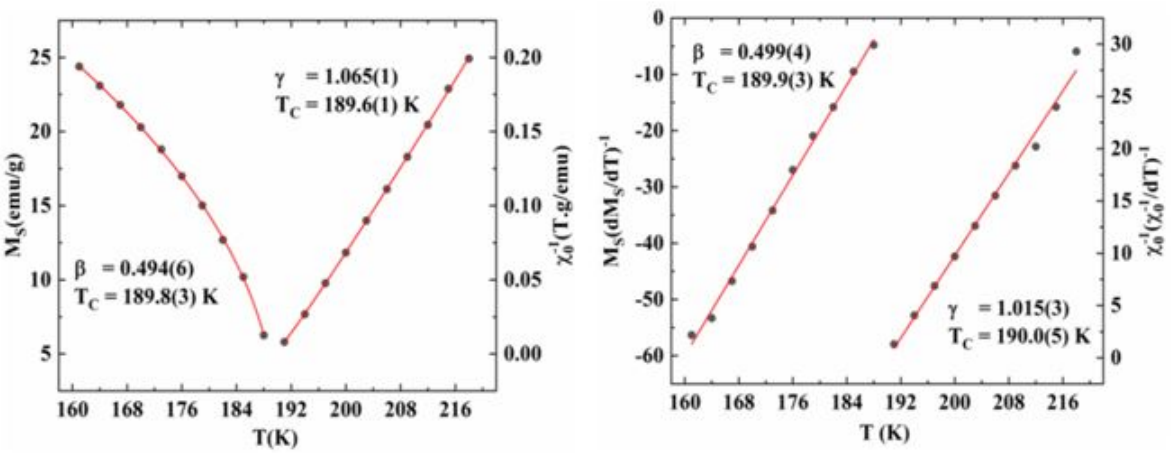

Fig. 8. (a) Temperature dependent spontaneous magnetization (M_S) and initial susceptibility(χ_0^{-1}) for $Mn_{4.5}Ni_{0.5}Sn_3$ alloy; (b) KF method plots of M_S and inverse initial susceptibility(χ_0^{-1})

KF method yields two straight lines below and above T_C. By fitting Eqn. (6 & 7), as shown in Fig. 8(b), one would obtain the parameters as, $\beta = 0.499(4)$ with $T_C = 189.9(3)$ K and $\gamma = 1.015(3)$ with $T_C = 190(5)$ K which are in consonance with those obtained from MAP method.

The significance of the critical exponents β, γ and δ are as follows: (i) β signifies the growth of ordered moments below T_C, with decrease in its magnitude, the rate of moment ordering raises. (ii) γ indicates the magnetic susceptibility divergence at T_C, smaller the γ value sharper the divergence. (iii) δ is connected with the curvature of $M(B)$ at T_C, as δ declines, the moments slowly saturate and hence a lesser curvature is seen in $M(B)$ plots [32]. δ can be calculated directly by plotting natural logarithm of high field isothermal magnetization near T_C or by Widom scaling relation [33],

$$\delta = 1 + \frac{\gamma}{\beta}. \tag{8}$$

From the β and γ values obtained using KF and MAP method, we have calculated δ values as 3.034 and 3.155, respectively. Also, from critical isotherm, δ can be attained by fitting the following relation [30],

$$M_{T_C} = DB^{(1/\delta)} \tag{9}$$

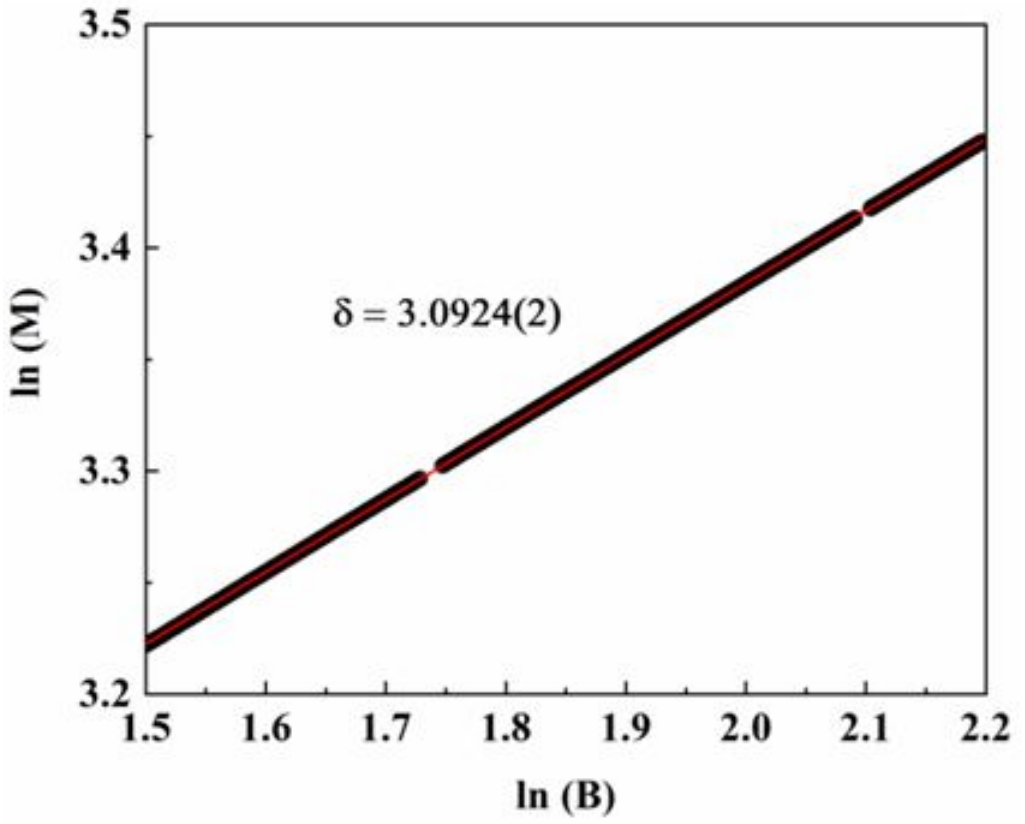

Fig. 9. Isothermal magnetization of $Mn_{4.5}Ni_{0.5}Sn_3$ alloy near TC in log-log scale. The red line represents the fitting of Eq. (9)

δ value acquired from the above fit is in accordance with theoretical value calculated using Widom scaling relation. Table II summarizes the critical exponents of our sample along with the previously reported data.

In addition, the critical exponents can be verified by scaling equation [34],

$$M(B,\varepsilon) - \varepsilon^{\beta} f_{\pm}\left(B/\varepsilon^{\beta+\gamma}\right), \tag{10}$$

where ε is the reduced temperature, $\varepsilon = (T - T_C)/T_C$, f_+ and f_- are regular analytical function at $T > T_C$ and $T < T_C$, respectively. As shown in Fig. 10, the magnetization $\left(M|\varepsilon|^{-\beta}\right)$ and magnetic field are renormalized using β and γ values obtained from KF method and plotted. It can be seen that the plots are merged into two branches one below T_C and above T_C in consistent with scaling hypothesis. It confirms the reliability and the validity of critical exponents of our system.

Table II: Comparison of critical exponents derived for $Mn_{4.5}Ni_{0.5}Sn_3$ alloy and other reported results of Mn-Sn systems with the theoretical models.

Materials/Models	Technique	T_C (K)	β	γ	δ	Reference
Mean-field model	Theory	/	0.5	1.0	3.0	[28]
3D-Heisenberg model	Theory	/	0.365	1.336	4.80	[28]
3D- Ising model	Theory	/	0.325	1.241	4.82	[28]
Tricritical mean-field model	Theory	/	0.25	1.0	5.0	[29]
$Mn_{4.5}Ni_{0.5}Sn_3$	MAP	189.7	0.494	1.065	/	This work
	KF	190	0.499	1.015	/	This work
	CI (cal)	/	/	/	3.034	This work
	CI (exp)	/	/	/	3.092	This work
$Mn_{0.94}Sn_{0.06}CoGe$	MAP	291.6	0.453	0.962	3.122	[35]
	KF	292	0.453	0.950	3.097	
$MnCo_{0.08}Sn_{0.02}Ge$	KF	266	0.472	.953	3.017	[16]
$Mn_{1.9}Sn$	MAP	207.7	0.408	1.044	3.559	[36]
	CI	208	/	/	3.53	
$Mn_{39.5}Fe_{8.5}Ni_{41}Sn_{11}$	MAP	308	0.48	1.07	3.96	[4]

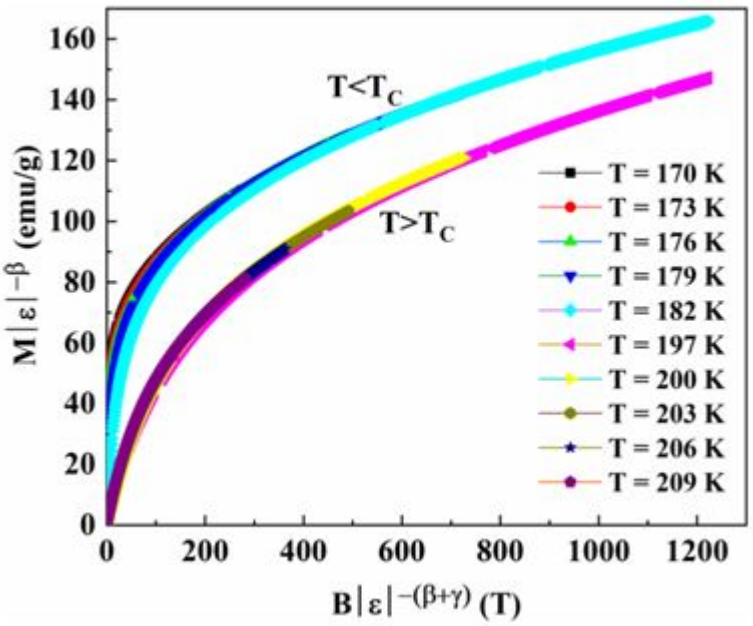

Fig. 10. Scaling plots of $Mn_{4.5}Ni_{0.5}Sn_3$ alloy

3.2 Mangentocaloric Effect:

Using isothermal magnetization data measured at various temperatures, the isothermal magnetic entropy change ($-\Delta S_M$) has been calculated from Maxwell equations. The calculated MCE attains a maximum value of 1.87 J/kg K and 2.88 J/kg K at T_C in $\Delta B = 5T$ and $9T$, respectively (Fig. 11).

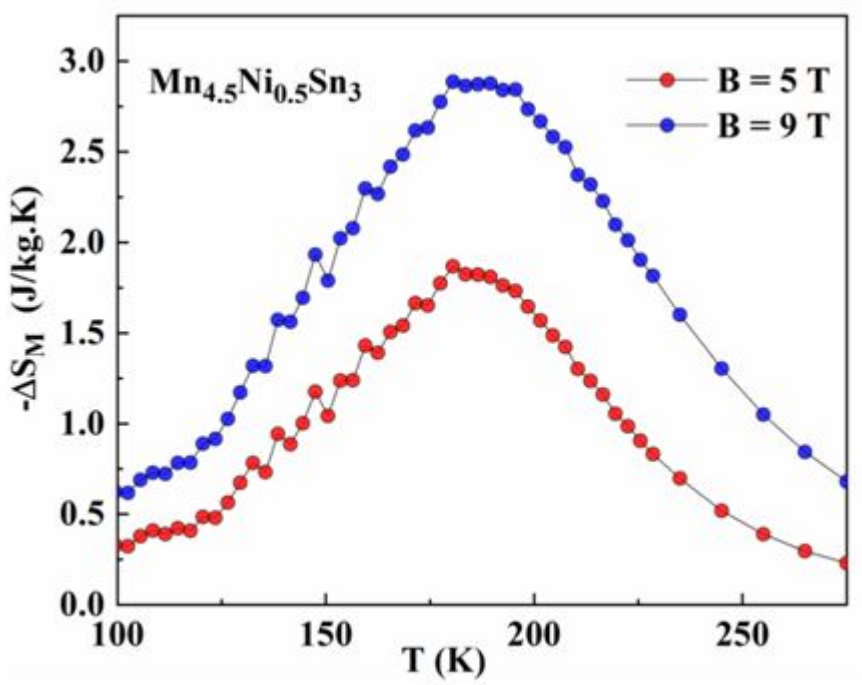

Fig. 11. Magnetic entropy change of $Mn_{4.5}Ni_{0.5}Sn_3$ alloy

Even though the magnitude is comparable with other Mn-based alloys, the operational temperature range is far better. Relative cooling power (RCP), a figure of merit of MCE materials, can be calculated using Wood and Potter method from the relation, $RCP = -\Delta S_M^{max} \times \Delta T_{FWHM}$, where $-\Delta S_M^{max}$ is maximum entropy change and ΔT_{FWHM} is full width at half maximum. The RCP of the alloy has been estimated from $-\Delta S_M$ curves, and it is found to be 160 J/kg and 302 J/kg for 5 T and 9 T respectively. The high value of RCP is mainly due to the enhancement of ΔT_{FWHM}, which is 86 K and 105 K in an applied magnetic field of 5 T and 9 T, respectively. The results gathered from $-\Delta S_M$ curves are compared with other Mn-based compounds in Table III.

Table III: Comparison of isothermal magnetic entropy change ($-\Delta S_M$), working temperature span (ΔT_{FWHM}) and relative cooling power (RCP) of $Mn_{4.5}Ni_{0.5}Sn_3$ alloy with other Mn based alloys

Material	$-\Delta S_M$ (0-5 T) (J/kg.K)	T_{cold} (K)	T_{hot} (K)	ΔT_{FWHM} (K)	RCP (J/Kg)	Reference
$(Mn_{1-x}Fe_x)_5Sn_3$	2.2	255.5	310	54.5	120	[14]
$Ni_{42}Co_8Mn_{30}Fe_2Ga_{18}$	31	203	207	4	124	[37]
$Ni_{48}Mn_{39}Sn_{11}Ge_2$	14.64	245	255	10	146	[38]
$Ni_{53}Mn_{26}Ga_{22}$	30	353	356	3	90	[39]
$Mn_{4.5}Ni_{0.5}Sn_3$	1.87	138	224	86	160	Present work

According to Oesterreicher and Parker, from the field dependent magnetic entropy change, the local exponent n can be studied based on the following relation [40],

$$\Delta S_M \propto B^n \tag{11}$$

n value should be around 2/3 for ferromagnetic materials in the vicinity of Curie temperature [19]. Fig. 12 displays the log-log scale of ΔS_M^{max}, where the solid line represents the fit of Eqn.11. The value of local exponent is 0.758. Further the critical exponents and the local exponent are related as [40],

$$n = 1 + \frac{\beta - 1}{\beta + \gamma} \tag{12}$$

The procured values of n are 0.675 and 0.670 for MAP and KF method respectively which is in good agreement with the value calculated from experimental technique.

A universal curve proposed by Franco et al [41] is a new criterion to analyze the nature of magnetic transition. On plotting normalized entropy against rescaled temperature for various fields, all the data points should fall into a single curve for second order transition materials. The rescaled temperature axis, θ , is given by,

$$\theta = \begin{cases} -(T - T_{pk})/(T_{r1} - T_{pk}); & T_{r1} \leq T_{pk} \\ (T - T_{pk})/(T_{r1} - T_{pk}); & T_{r2} > T_{pk} \end{cases} \tag{13}$$

Here Tr_1 and Tr_2 are two reference temperatures corresponding to $0.5 \times \Delta S_M^{pk}$. It should be noted from Fig. 13, that all the data points have collapsed into a single curve revealing the second order nature of magnetic transition. Lorentzian function used to fit the observed phenomenological curve is defined as [42]

$$\Delta S' = \frac{a}{b + (\theta - c)^2} \tag{14}$$

Here a, b and c represents free parameters and their values are 1.006, 0.9106 and 0.0674 respectively.

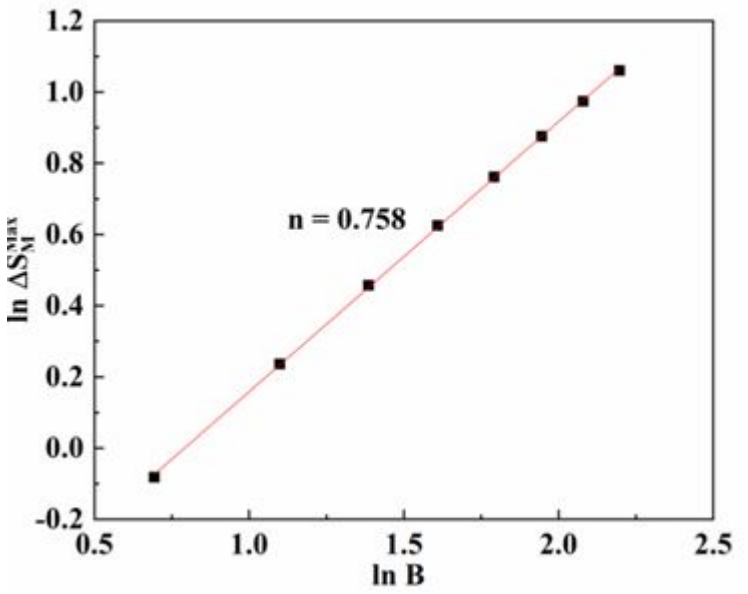

Fig. 12. ln SM vs ln B plot of $Mn_{4.5}Ni_{0.5}Sn_3$ alloy

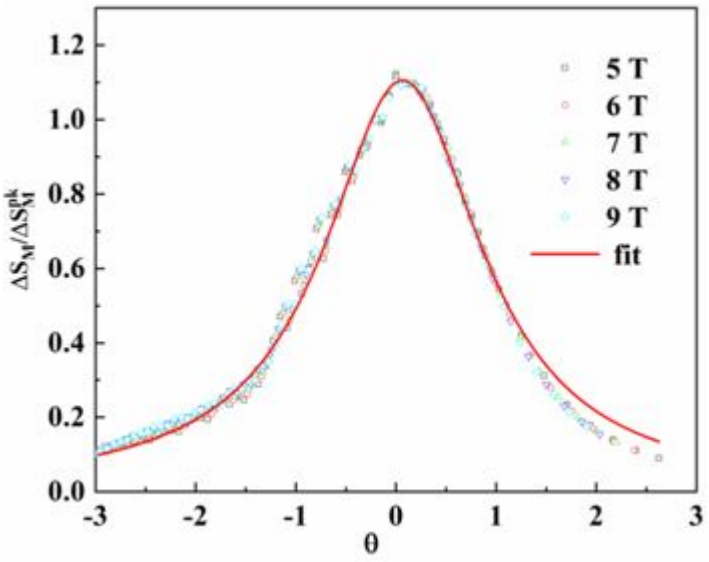

Fig. 13. Universal behavior of $Mn_{4.5}Ni_{0.5}Sn_3$ alloy with Lorentz function fit

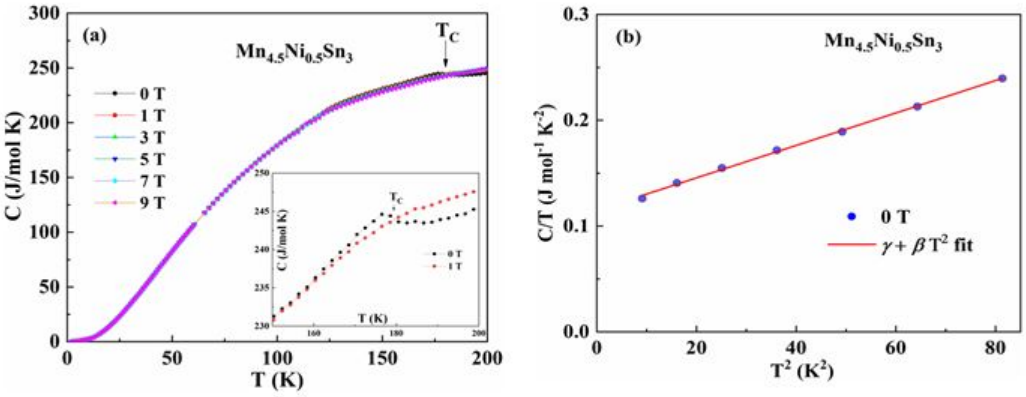

Fig. 14. (a) Temperature dependent heat capacity of $Mn_{4.5}Ni_{0.5}Sn_3$ alloy (main panel). Lower inset displays behavior of heat capacity near TC; (b) Temperature dependence of C/T vs T2 at low temperatures.

The main sector of Fig. 14(a) demonstrates the variation of heat capacity with respect to the temperature. Around T_C, a λ-like anomaly can be seen and gradually broadens and shifts towards high temperature as applied magnetic field is hiked (see inset of Fig. 14(b)).

By plotting $C/T\ vs\ T^2$ at very low temperatures, we can obtain electronic (γ_c), and lattice (β_c) heat capacity coefficients, using the relation $C/T = \gamma_c + \beta_c T^2$. From the fit, the values of γ_c and β_c are found to be 114.8 mJ mol^{-1} K^{-2} (intercept) and 1.53 mJ mol^{-1} K^{-4} (slope), respectively. The high value of γ_c indicates the moderate heavy Fermion characteristics of the $Mn_{4.5}Ni_{0.5}Sn_3$ alloy. By using the value of β_c, the Debye temperature θ_D can be determined from the below equation [43],

$$\beta_c = \frac{12\pi^4}{5} nR \left(\frac{1}{\theta_D}\right)^3. \tag{15}$$

Here n and R are the number of atoms per f.u. and universal gas constant respectively. The estimated value of θ_D is 216 K. At Fermi level, the relation between γ_c and the density of states is given by [43],

$$\gamma = \frac{\pi^2 N_A k_B^2}{3}(1+\lambda)N(E_F), \tag{16}$$

where N_A, k_B, λ and $N(E_F)$ are Avagadro number, Boltzmann constant, mass enhancement coefficient and density of states per formula unit at Fermi energy respectively. The obtained value of $(1+\lambda)N(E_F)$ is 48.6 states eV^{-1}.

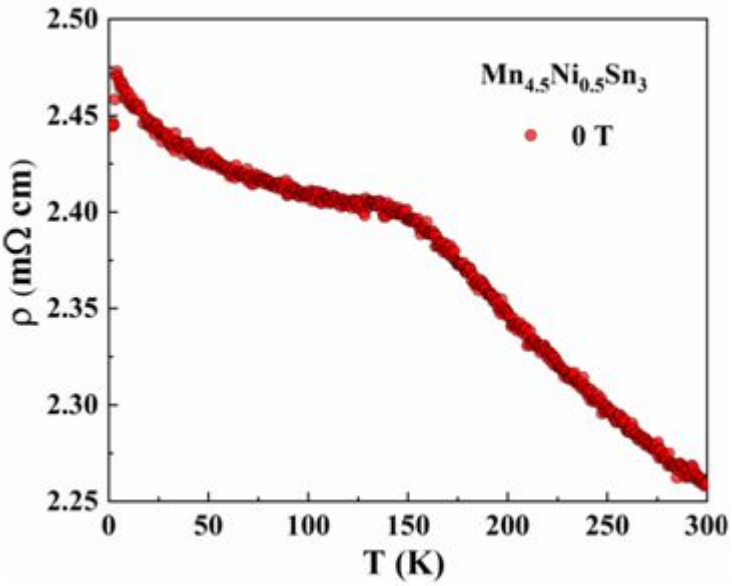

Fig. 15. Temperature dependent electrical resistivity of $Mn_{4.5}Ni_{0.5}Sn_3$ alloy

The resistivity plot of $Mn_{4.5}Ni_{0.5}Sn_3$ alloy demonstrates a negative temperature coefficient of resistivity (TCR). Generally, in transition metal based alloys, negative TCR arises due to strong impurity scattering [44]. This factor might have also caused the enhanced Sommerfeld coefficient leading to the moderate heavy Fermion behavior of the alloy. It is a well-known fact that, the magnitude of γ_c which is directly correlated with the effective mass of electrons in the system depends on three factors such as, interaction between conduction electrons with periodic lattice, conduction electrons with phonons and interaction within the conduction electrons. Even with the above facts considered, the origin of high γ_c in this system is still unclear. In addition, there is a kink around T_C, which is due to the enhancement of spin correlated scattering [26]. Since, the room temperature resistivity is so high when compared to Mott-loffe-Regel value, 308 $\mu\Omega$ cm, the alloy can be claimed to be a bad metal [45].

4 Conclusion

$Mn_{4.5}Ni_{0.5}Sn_3$ alloy undergoes ferromagnetic transition at 180 K, and a magnetic spin freezing transition at 21 K due to its reentrant spin glass characteristics. The positive value of Landau coefficient, $B(T_C)$ confirms second order nature of the ferromagnetic transition. In addition the master curve behavior and the scaling hypothesis further support the above claim. The critical exponents β, γ and δ obtained using several methods coordinate well with those corresponding to mean field

model revealing the presence of long range interaction among the moments. From the behavior of $\rho(T)$ curve, the existence of strong impurity scattering is evident implying that the material is a bad metal. This has been reflected back in the effective mass of the electron thereby a large electronic coefficient of 114.8 mJ mol^{-1} K^{-2} is observed. Further, as a magnetic refrigerant, it is a potential candidate as it shows a wide temperature span of 86 K, which gives a great boost to RCP value.

Acknowledgements

The author thanks UGC DAE Consortium, Indore for Scientific research for the sanction of project (CSR-IC/CRS-150/2015-16/07). The help rendered by Mr. Nilesh Kulkarni and Mrs. Bhagyashree Chalke, Department of Condensed Matter Physics, Tata Institute of Fundamental Research, Mumbai, India in structure and compositional measurements are highly acknowledged. The author thanks Prof, Marian Rieffers for facilitating magnetization, heat capacity and resistivity measurements. This work is the result of the Project implementation: University Science Park TECHNICOM for Innovation Applications Supported by Knowledge Technology, ITMS: 26220220182, supported by the Research & Development Operational Programme funded by the ERDF and also by VEGA 1/0611/18, 1/0956/17 and APVV-16-0079.

References

1. B. Dahal, C. Huber, W. Zhang, S. Valloppilly, Y. Huh, P. Kharel, and D. Sellmyer, Journal of Physics D: Applied Physics 52, 425305 (2019).

2. S. Singh, L. Caron, S. W. D'Souza, T. Fichtner, G. Porcari, S. Fabbrici, C. Shekhar, S. Chadov, M. Solzi, and C. Felser, Advanced Materials 28, 3321 (2016).

3. G. Engdahl, Handbook of Giant Magnetostrictive Materials (Academic Press, San Diego, 2000).

4. S. Ghosh, A. Ghosh, and K. Mandal, J. Alloys Compd. 746, 200 (2018).

5. E. Bruck, Journal of Physics D: Applied Physics 38, R381 (2005).

6. Y.-K. Fang, J.-C. Yeh, W.-C. Chang, X.-M. Li, and W. Li, J. Magn. Magn. Mater 321, 3053 (2009).

7. P. E. Markin, N. V. Mushnikov, E. G. Gerasimov, A. V. Proshkin, and A. S. Volegov, The Physics of Metals and Metallography 114, 893 (2013).

8. J. Q. Zhao, H. X. Zhu, C. L. Zhang, Y. G. Nie, H. F. Shi, E. J. Ye, Z. D. Han, and D. H. Wang, J. Alloys Compd. 735, 959 (2018).

9. A. Quetz, T. Samanta, I. Dubenko, M. J. Kangas, J. Y. Chan, S. Stadler, and N. Ali, J. Appl. Phys. 114, 153909 (2013).

10. E. Liu, W. Wang, L. Feng, W. Zhu, G. Li, J. Chen, H. Zhang, G. Wu, C. Jiang, H. Xu, and F. de Boer, Nature Communications 3, 873 (2012).

11. K. Deepak and R. V. Ramanujan, J. Alloys Compd. 743, 494 (2018).

12. J. Liu, X. M. You, B. W. Huang, I. Batashev, M. Maschek, Y. Y. Gong, X. F. Miao, F. Xu, N. van Dijk, and E. Bruck, Phys. Rev. Mater. 3, 084409 (2019).

13. F.-q. Zhao, W. Dagula, O. Tegus, T. Gortenmulder, H. Buschow, and K. Buschow, IEEE Trans. Magn. 41, 3754 (2005).

14. J. H. Xu, X. M. Liu, Y. H. Xia, W. Y. Yang, H. L. Du, J. B. Yang, Y. Zhang, and Y. C. Yang, J. Appl. Phys. 113, 17A921 (2013).

15. J. H. Xu, Y. H. Xia, W. Y. Yang, H. L. Du, J. B. Yang, C. S. Wang, J. Z. Han, S. Q. Liu, and Y. C. Yang, J. Appl. Phys. 113, 17E111 (2013).

16. X. Si, K. Zhou, R. Zhang, J. Qi, and Y. Liu, Phys. Lett. A 381, 2850 (2017).

17. X. Si, Y. Liu, Y. Shen, W. Yu, X. Ma, Z. Zhang, Y. Xu, and T. Gao, Journal of Materials Science 53, 3661 (2017).

18. X. Si, K. Zhou, R. Zhang, Y. Liu, and J. Qi, J. Appl. Phys. 121, 113902 (2017).

19. X. Si, Y. Liu, Y. Shen, W. Yu, X. Ma, Z. Zhang, Y. Xu, and T. Gao, Intermetallics 93, 30 (2018).

20. M. Halder, S. M. Yusuf, and A. K. Nigam, J. Appl. Phys. 110, 113915 (2011).

21. A. K, S. S, R. U. D, A. Dzubinska, M. Reiffers, and N. R, J. Appl. Phys. 127, 053901 (2020).

22. J. Rodrguez-Carvajal, Physica B 192, 55 (1993).

23. N. S. Satya Murthy, R. J. Begum, B. S. Srinivasan, and M. R. L. N. Murthy, Phys. Lett. 15, 225 (1965).

24. J. Huang, J. Xiang, C. Zhi, X. Z. Wang, and X. L. Hou, Advanced Materials Research 299-300, 520 (2011).

25. Z. S. Zhang, X. H. Luo, Y. Song, K. Liu, S. C. Ma, C. C. Chen, Y. X. Zhang, H. Zeng, X. W. Zhao, Q. Z. Jiang, S. U. Rehman, and Z. C. Zhong, Phys. Lett. A 383, 2229 (2019).

26. I. Ahmad Shah, G. Xu, N. ul Hassan, M. Arif, Y. You, J. Liu, Y. Gong, X. Miao, and F. Xu, J. Magn. Magn. Mater 465, 360 (2018).

27. A. Arrott and J. E. Noakes, Phys. Rev. Lett. 19, 786 (1967).

28. M. Seeger, S. N. Kaul, H. Kronmuller, and R. Reisser, Phys. Rev. B 51, 12585 (1995).

29. K. Huang, Statistical Mehcanics, 2nd ed. (Wiley, New York, 1987).

30. H. E. Stanley, Introduction to Phase Transitions and Critical Phenomena (Oxford University Press, New York, 1971).

31. J. S. Kouvel and M. E. Fisher, Phys. Rev. 136, A1626 (1964).

32. M. Halder, S. M. Yusuf, M. D. Mukadam, and K. Shashikala, Phys. Rev. B 81, 174402 (2010).

33. B. Widom, J. Chem. Phys. 43, 3898 (1965).

34. H. E. Stanley, Rev. Mod. Phys. 71, S358 (1999).

35. X. Si, K. Zhou, R. Zhang, Y. Liu, and J. Qi, Phys. Lett. A 381, 1693 (2017).

36. W. J. Feng, L. Gao, X. L. Fan, C. M. Li, S. Wang, X. Hong, X. S. Sun, M. Gao, and Y. F. Deng, Materials Research Express 6, 036102 (2018).

37. A. K. Pathak, I. Dubenko, H. E. Karaca, S. Stadler, and N. Ali, Appl. Phys. Lett. 97, 062505 (2010).

38. X. D. Sun, C. Jing, C. Q. Liu, M. F. Ye, Y. S. Huang, and G. J. Zhang, Phase Transit 92, 13 (2019).

39. Z. B. Li, Y. D. Zhang, C. F. Sanchez-Valdes, J. L. S. Llamazares, C. Esling, X. Zhao, and L. Zuo, Appl. Phys. Lett. 104, 044101 (2014).

40. V. Franco, J. S. Blazquez, and A. Conde, Appl. Phys. Lett. 89, 222512 (2006).

41. V. Franco, A. Conde, V. Provenzano, and R. D. Shull, J. Magn. Magn. Mater 322, 218 (2010).

42. P. T. Phong, N. V. Dang, L. V. Bau, N. M. An, and I. J. Lee, J. Alloys Compd. 698, 451 (2017).

43. Q. Recour, T. Mazet, and B. Malaman, J. Appl. Phys. 105, 033905 (2009).

44. P. Kharel, W. Zhang, R. Skomski, S. Valloppilly, Y. Huh, R. Fuglsby, S. Gilbert, and D. J. Sellmyer, Journal of Physics D: Applied Physics 48, 245002 (2015).

45. T. Ghosh, S. Agarwal, and P. K. Mukhopadhyay, J. Magn. Magn. Mater 418, 260 (2016).